PROCEEDINGS, 46th Workshop on Geothermal Reservoir Engineering
Stanford University, Stanford, California, February 15-17, 2021
SGP-TR-218

Geothermal Design Tool (GeoDT)

Luke P. Frash

Los Alamos National Laboratory, PO Box 1663, Los Alamos, NM 87545

lfrash@lanl.gov

Keywords: Enhanced Geothermal Systems, Discrete Fracture Network, Geothermal Power, Well Design, Site Planning

ABSTRACT

Advanced modelling capabilities are currently available to evaluate hydraulic fracture stimulation, fracture network fluid flow, subsurface fluid-rock heat and mass transfer, multi-well flow dynamics, geomechanical coupling, geochemical coupling, and long-term electrical power production. While all these components should be considered together in the optimized design of wells and well fields, no models are yet known to us that couple all these processes efficiently and intuitively enough for timely making during ongoing projects. Our aim here is not to develop a new model to add to the existing collection of high-fidelity and high-performance codes. Instead, our goal is to develop a fast decision making assistance tool. This tool targets the early stages of new field development, when uncertainties are very high and data is sparse to non-existent. By cruel coincidence, this early development timeframe is also when informed decisions are most critical to the success of a geothermal development project. To achieve our goal, we must focus on high-priority controllable parameters such as well placement. The site parameters are limited to those that can be reasonably characterized by common low-cost methods or are defaulted to estimations based on published values. A key element of our approach is to start by including the complexity of what can occur in the natural environment to avoid oversimplifications that would yield misleading or incorrect guidance for decision making.

1. INTRODUCTION

Our decision making tool is motivated, in part, by recent experience gained from the EGS Collab Project at the Sanford Underground Research Facility (SURF) in Lead, South Dakota (Kneafsey et al., 2020). This decameter scale project involved all phases of Enhanced Geothermal System (EGS) reservoir development from site selection through to long-term multi-well flow circulation. A fundamental two-part lesson learned from this work was: (1) the complexity of flow through naturally fractured rock has very real effects on the final performance of a system and (2) there is a strong temptation to use simplified models for site design when site data is lacking. Combined, this can easily lead to a misleading sense of confidence in the early development stages when key decisions are being made.

To provide a tangible context to the above lesson, let us consider the following scenario. A pilot vertical well into a new geothermal field indicates negligible natural fracturing, negligible rock permeability, and high-integrity monolithic rock. Diagnostic hydraulic fracture tests estimate a horizontal minimum principle stress that is due north at 24 MPa and an overburden stress of 44 MPa. These observations justify the modeling assumption of negligible matrix leak-off and the expectation of vertical hydraulic fractures. They also justify the assumption of negligible natural fractures at this site. Based on this, an effective heat extraction system could use multiple hydraulic fracture stages between two horizontal wells. More than two horizontal wells would not be justifiable because the stimulation models would predict consistent trends for fracture growth, most likely upward trends (Fischer et al., 2009). Thus, drilling of the two wells begins.

Upon completing the first horizontal well, new data emerges that the site is intensely fractured with complex conjugate vertical joint sets. Some fractures are naturally flowing and large at greater than 10 mm aperture. Meanwhile, the drilling rig is on site with a drilling plan for the two wells that was approved only after months of deliberation. Furthermore, the new data does not identify the locations of the flowing natural fractures, predominantly because the fracture lengths are unknown. No equipment is on-hand to better characterize the fractures. Now, the clock is running, downtime is expensive, and the new equipment and analysis effort needed to recharacterize and redesign the site will take weeks or longer and may, or may not, yield significant changes to the drilling plan. Adding to the difficulty is the silence from key contractors who fear legal repercussions should they provide incorrect guidance due to rushed decision making. A decision must be made on whether to continue with the original plan or to halt operations to reassess, but not without expense.

This scenario posed here is similar to the experience of the EGS Collab Team when developing Experiment 1. The arguably most rational decision would be to continue per the approved plan and avoid lengthy and costly delays. The consequences of this decision for geothermal production would not be known until long after drilling was completed. In hindsight, if the initial planning had assumed more complex site scenarios that included what was encountered, perhaps better-informed solutions would have been available. For industry, this detailed early planning contradicts with the rational desire to use the cheaper and faster simplified models for site design.

Here, we introduce a geothermal design tool, still in development, that aims to prepare decision makers for the complex reality of EGS and to better equip them to make better informed decisions when time is of the essence. Our goal is a desktop model that can solve 20+ year production scenarios in mere minutes. We expect that the model will require: (1) three-dimensional discrete fracture networks, (2) multiple wells, (3) fracture stimulation, (4) realistic default property assumptions for complex and uncertain site properties, (5) control over key decisions such as well placement, and (6) long-term electrical-power production prediction. With such a tool, it could be possible to create adaptive plans for high-performance and reliable development of new geothermal resources.

2. NUMERICAL METHODS

The workflow of our modeling tool begins with model parameterization and ends with an estimate of flow and enthalpy inputs and outputs converted to a net electrical power generation estimate. Properties of the site start with default values that cover a maximum of possibilities and these values can later be refined as new data becomes available. The model's general workflow is depicted in Figure 1. This workflow foregoes the complex coupling of hydro-thermo-chemo-mechancial effects and instead favors a fast linear workflow. This will introduce errors relative to high-fidelity coupled solvers. However, we suspect that many of these errors will be secondary to the variability inherent to uncertain flow through rock fracture networks.

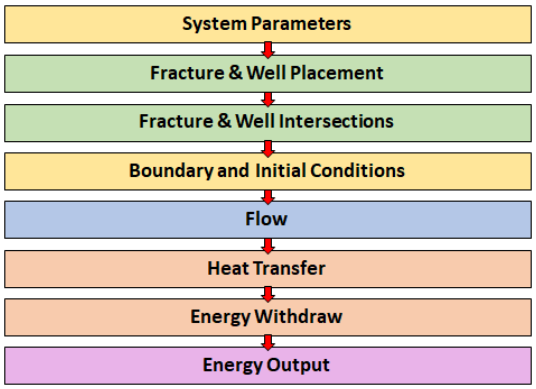

Figure 1: General workflow for flow and heat transfer modeling in multi-well leaky fracture-networks.

2.1 Fracture and Well Placement

We use line segments to represent wells. Optimized well designs and locations are of the utmost importance when developing a site and are thereby a key user input for modeling. Wells can be cased, open, or cased and perforated, each option having its own benefits for flow control. In addition, for more exotic systems, wells can contain some intervals that are used for injection while other intervals of the same well can be used to produce fluid. At the boundaries, the wells are assigned a set flow rate or pressure condition in addition to a temperature for any injected fluid. These wells will become fluid producers, injectors, or a mixture of both as determined by the fluid flow solver.

We use planar circles to represent fractures in three-dimensional space. The center position, length, strike, and dip of these fractures are specified directly or via a statistical distribution that can be determined using well logs or estimated based on prior experiences. By default, we shall assume that natural fractures can exist anywhere, unless proven otherwise. At present, the model uses assumed geometries for any hydraulic fractures that are to be stimulated from any of the wells. In the near future, we plan to add a well stimulation module that will predict hydraulic fracture dimensions as a function of injection rate and total injected volume.

2.2 Fracture and Well Intersections

To speed-up analysis and improve the ease of visualizing and interpreting three-dimensional flow networks, we model the fracture and well system using a network of pipes and nodes (Figure 2). Pipes represent flow channels through fractures or wells. Nodes represent well-well, well-fracture, fracture-fracture, well-boundary, and fracture-boundary intersections. Every fracture that connects to the flow network includes one node at its center point. This fracture-center node is used to calculate fracture pressure as required to assess shear slip criteria. Furthermore, using a common center node prevents unrealistic crisscrossing flow paths that could be otherwise be computed to have unequal pressures at intersections when using our flow solver. The node for the intersection between two planes is set at the midpoint of the intersected chord that is common to both fractures.

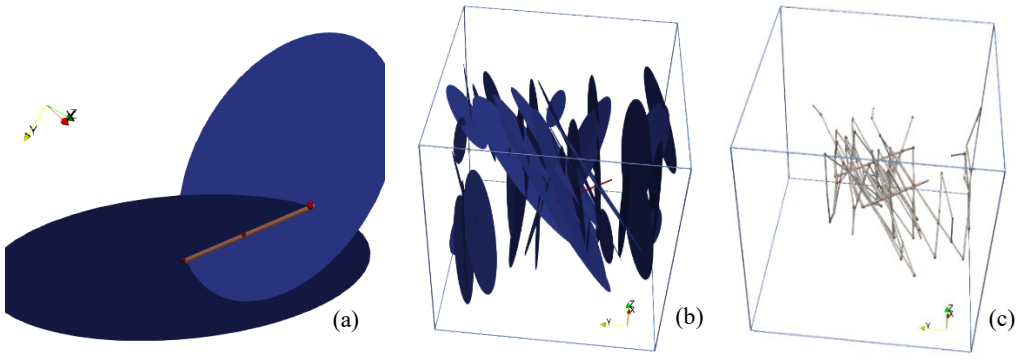

Figure 2: (a) Intersection line of two planes. The midpoint of this line becomes a node in the pipe flow network. The length of the intersection line (yellow) is used for the characteristic width of the fracture flow path. (b) An example fracture network (blue) having two wells (red). (c) Pipe and node flow network for the fractures and wells. Fractures intercepting the cubical domain boundary are handled as a special case to enable modeling leaky-boundary effects.

We identify intersections sequentially, starting from the wells, such that they can be thought of as a first, second, third, etc. set in a series. The intersection algorithm will ignore isolated fractures and will not duplicate pipes between the same nodes. The resulting pipe and node network serves as the mesh for our flow and heat transport solvers.

It is known that the near-well flow zone can incur significant pressure losses in short distances, a process often referred to as perforation friction, near wellbore tortuosity, and/or skin factor. Therefore, we insert a pipe 'choke' segment at the well and fracture intersections to enable inclusion of this important effect (Figure 3). The width of this 'choke' is set at the circumference of the well (π*D_w) and the length is set at a factor of the well's diameter (3*D_w). We use a rule-of-thumb value of 3 for this factor because localized perturbations around a hole in a plate become negligible at less than 1% beyond 9 radii from the center of the well (Valko and Economides, 1996). A more accurate solution for this effect is attainable using more advanced flow solvers. However, we expect heterogeneity will induce significant variability that will dominate the uncertainty in this factor, therefore we include variability in this factor in our model.

For the boundary, we require a leaky far-field condition to avoid over-predicting fluid containment within a natural fracture network. A leaky boundary emulates scenarios such as fractures linking to permeable faults or penetrating into permeable rock formations. Thus, a no-flow boundary condition is not appropriate. A constant pressure boundary condition would be the standard alternative. However, this option could introduce unrealistically high flow rates if a high-permeability fracture happened to connect to the boundary. Instead, we apply a hybrid boundary condition having long fracture flow pathways that link to constant pressure nodes (Figure 3). Just as for the fractures, the properties of these pathways are uncertain and estimated stochastically.

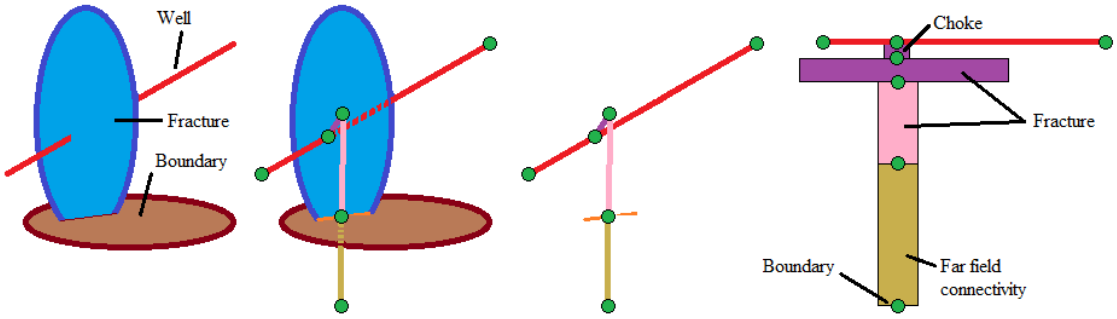

Figure 3: Pipe and fracture intersections converted to a pipe and node mesh. The pipe and fracture intersection adds a 'choke' segment in the flow path. The fracture (blue) intersection with the boundary (brown) is a special case that extends the flow path to the far-field (100x domain size).

2.3 Boundary and Initial Conditions

The domain's boundary nodes are set at a constant pressure condition. This permits far field fluid flow to simulate leaky fracture networks. The initial pressure and temperature conditions are set based on provided site parameters (e.g., depth and temperature gradient). Injection and production wells can be specified with either a constant pressure or constant flow rate boundary condition. Typically, injection well flow rate is assigned and a production well pressure is assigned by the user. This choice provides good model stability and assists in the characterization and understanding of the complete well and fracture system.

2.4 Pipe and Fracture Properties

Firstly, water is the typical fluid of interest for subsurface flow and transport. Therefore, this will be the working fluid for our model. For pipe flow, the Hazen-Williams equations enables quick estimation of water pipe fictional losses. For fracture flow, frictional losses can be estimated using the effective cubic law. This differs from the ideal parallel plate law by including an aperture reduction factor to account for non-ideal geometry. It is rare to have information about actual fracture permeability, aperture, length, or location in the field, but these terms are crucial to connectivity and transport. To address this, we can use stochastic fracture placement and aperture-length scaling relationships that estimate the range of potential fracture properties that could occur in rock (Frash et al., 2020). In addition, our model must be solvable within the constraints of computer precision. It can be shown that a solvable fracture flow network that uses nodal pressures as the state variable to estimate flow rates is subject to numerical limitations for large and small apertures. For fractures in the 1 to 10000 m length scale and standard 64-bit precision, these limits for effective hydraulic aperture will be in the range of 0.05 mm to 5.0 mm. Fractures with apertures smaller than this range will have near-zero flow at large pressure gradients. Larger apertures will have excessively high permeability to the point that machine-precision becomes a limitation when estimating flow from pressure differences. Owing to these limitations, our models will assign all fractures an effective hydraulic aperture of 0.0002 m ±0.0001 m. This value achieves detectable pressure differences across fracture segments and treats tight fractures as negligible features for flow at the macro-scale.

2.5 Flow Solver

In this model, we solve for flow through the pipe and node network directly. To do this, we use the Newton-Raphson iterative solver (Jeppson, 1974) with some modifications to make the solution more universally applicable to fractures and pipes. Frictional losses in pipes are modeled using the Hazen-Williams equations for turbulent flow. Frictional losses in fractures are modeled using cubic law based on the effective hydraulic aperture (b_h) instead of the mechanical aperture (b_d). This is an important distinction because large fracture apertures can have negligible hydraulic apertures due to roughness. For our solution, node pressure is the state variable being solved.

We can estimate the fictional pressure head loss as follows:

$$h_f = \frac{\Delta P}{\rho g} \tag{A.1}$$

$$h_f = KQ^n \tag{A.2}$$

$$h_f = \begin{cases} \left(\frac{10.7L}{{C_{HW}}^{1.852} D^{4.87}}\right) Q^{1.852} & \text{if pipe} \\ \left(\frac{12\mu L}{b_h^3 w \rho g}\right) Q^{1.0} & \text{if fracture} \end{cases} \tag{A.3}$$

Where, L is pipe or fracture flow-path length, D is pipe inner diameter, C_{HW} is the Hazen-Williams friction coefficient (e.g., 130 for welded steel pipe or 80 for corroded steel pipe), Q is volumetric flow rate of liquid water, h_f is frictional pressure head loss, ΔP is lengthwise pressure gradient, ρ is fluid density, μ is fluid dynamic viscosity, b_h is effective hydraulic aperture, w is fracture width (not to be confused with length or aperture), and g is the gravitational constant. Next, we can solve for the flow rates as follows:

$$F_i = -\sum \left(\frac{H_j - H_i}{K_{ji}}\right)^{1/n_{ji}} \Bigg|_{inflow} + \sum \left(\frac{H_i - H_j}{K_{ij}}\right)^{1/n_{ij}} \Bigg|_{outflow} + Q_i \tag{B.1}$$

$$F_i = \sum \text{sign}(H_i - H_j) \left(\frac{|H_i - H_j|}{K_{ij}}\right)^{1/n_{ji}} + Q_i \tag{B.2}$$

$$\frac{\partial F_i}{\partial H_i} = \sum \frac{1}{n_{ij} K_{ij}} \left(\frac{|H_i - H_j|}{K_{ij}}\right)^{\frac{1}{n_{ij}} - 1} \tag{B.3}$$

$$\frac{\partial F_i}{\partial H_j} = \frac{-1}{n_{ij} K_{ij}} \left(\frac{|H_i - H_j|}{K_{ij}}\right)^{\frac{1}{n_{ij}} - 1} \tag{B.4}$$

$$D = \begin{bmatrix} \frac{\partial F_1}{\partial H_1} & \cdots & \frac{\partial F_1}{\partial H_n} \\ \vdots & \ddots & \vdots \\ \frac{\partial F_n}{\partial H_1} & \cdots & \frac{\partial F_n}{\partial H_n} \end{bmatrix} \tag{B.5}$$

$$H_{t0} = \begin{Bmatrix} H_1 = \text{rand}(H_0) \\ \vdots \\ H_n = \text{rand}(H_0) \end{Bmatrix} \tag{B.6}$$

$$[D]\{z\} = \{F\} \tag{B.7}$$

$$\{H_{t+1}\} = \{H_t\} - S\{z\} \tag{B.8}$$

$$Q_{ij} = \left(\frac{H_i - H_j}{K_{ij}}\right)^{\frac{1}{n_{ij}}} \tag{B.9}$$

Where, i and j are node numbers corresponding to pipe ends, t is an iteration counter, $t0$ is an initialization applicable to the first iteration only, H_0 is the initial formation pore pressure head, H_i is nodal pressure head, Q_i is a boundary condition flow rate that is positive for flow out of the node, and S is an overshoot damping factor that takes the value of 0.7 to achieve faster convergence. The iterative loop repeats J.2 through J.8 until the absolute maximum of the error term (z) is less than a goal value. The implementation of this code was validated against Jeppson's Chapter 6 Examples #1 and #2 (1974). This solution produced the same result as the examples, but with less iterations and reduced user effort.

2.6 Heat Transfer Solver

Many models of transient heat transfer in complex geometries will use meshed methods, such as finite differences. However, we seek a fast desktop-compatible solution that can support fracture apertures of less than 1 mm at length scales of at least 1 km for at least 20 yr of simulated operation. In addition, we desire a wall-time of 5 min or less to complete a model using one processor. While achieving this, we wish to avoid the challenges of large element counts that arise when modelling fractures in a three-dimensional continuum. Here, we describe a solution that achieves this goal.

Our heat transfer solution uses explicit time marching with an iterative heat flow solver for each time step (Figure 4). This predicts transient fluid-rock heat transfer to forecast thermal breakthrough times, short circuiting potential, and produced fluid enthalpy. Fluid flow is computed before this solver and is used as an input. The current implementation of our model does not directly address coupling between the fluid flow and heat transfer, so phase change effects are not directly resolved. In many EGS reservoirs, water will be in a compressed liquid state which is good for our solver, but solver accuracy will diminish if the water becomes a mixture of gas and liquid.

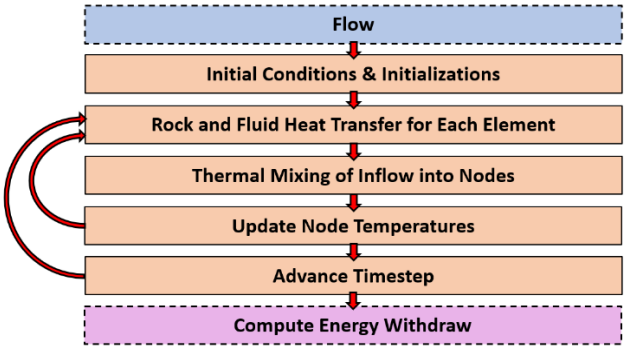

Figure 4: Workflow for our transient heat transfer solver with flow computed by the prior step.

Heat transfer during each timestep is solved for each pipe in the flow network (i.e., the flow paths through the wells and fractures). To do this, we use a pseudo-steady one-dimensional heat transfer approach (Figures 5 and 6) that combines the following:

1. An initial guess for a 'thermal radius' (r_d or R_{or}) where the rock temperature is not yet significantly changed from the initial state at the start of the timestep.
2. One-dimensional steady-state heat transfer for a round pipe or planar fracture based on this thermal radius and the mean of the nodal fluid temperatures at each end of the pipe.
3. Projected total energy exchange to/from the rock adjacent to this pipe over the timestep.
4. Updating the thermal radius based on the new fluid temperature and the total energy exchange from the rock.

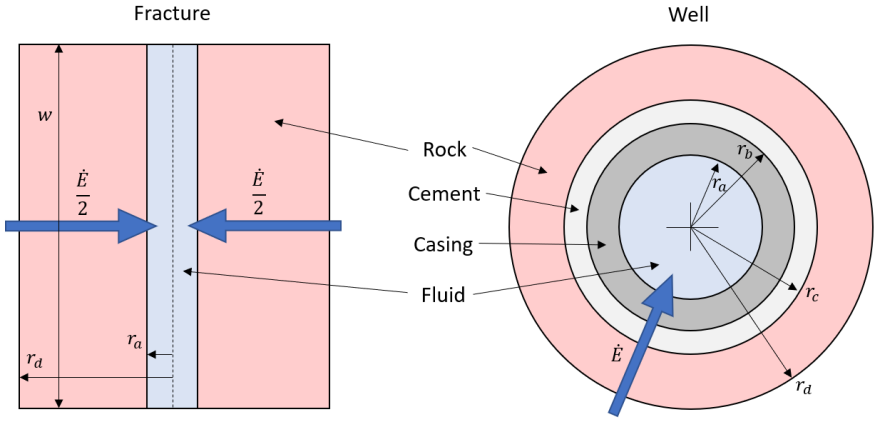

Figure 5: Heat transfer geometry for a planar fracture (left) and a radial cased well (right).

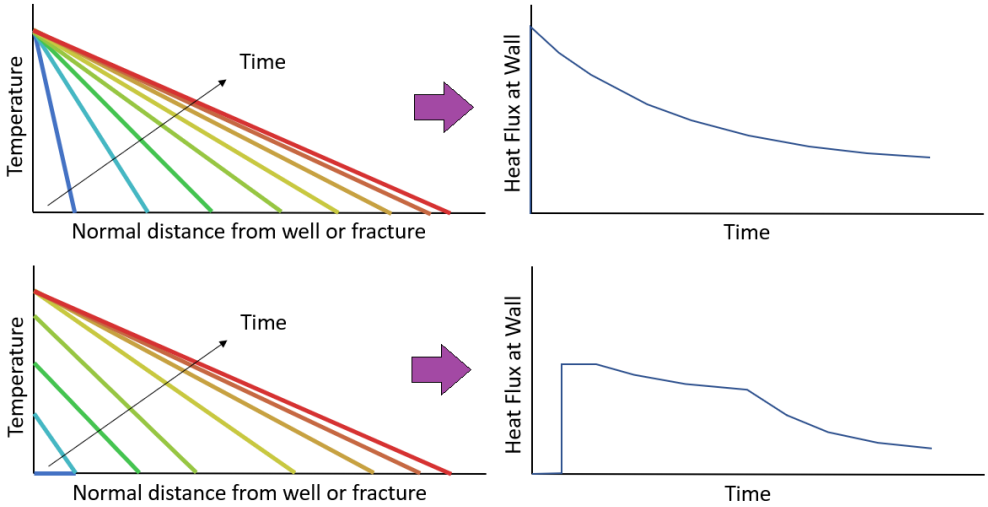

Figure 6: Scenarios we aim to solve with pseudo-steady heat transfer. (Top) A sudden increase or decrease in fluid temperature at a fracture face that will be followed by slowed heat transfer over time. (Bottom) Dynamic increases or decreases in fluid temperature at a fracture face that results in changing rates of heat transfer over time.

Evaluation of the heat transfer in the network of wells and fractures necessitates mixing flows and dividing flows at intersection nodes. To model this, we use conservation of energy and conservation of mass to mix the inflows into a node and then obtain a mixed enthalpy that is used for the outflow. The mixed enthalpy determines the fluid temperature at the node. Water temperature, enthalpy, pressure and steam quality are obtained from IAPWS97 (Cooper and Dooley, 2007) implemented into a python script (Romera, 2017). The nodal temperatures are solved by iteratively updating the pipe and node network until temperatures converge to less than 0.5 °C change.

2.6.1 Thermal Radius and Energy Storage:

For one-dimensional steady-state heat transfer through a series of materials (Lienhard and Lienhard, 2019):

$$\dot{E} = UA\Delta T \tag{C.1}$$

$$\frac{1}{U} = \sum \frac{1}{h_c} + \sum \frac{L}{k} \tag{C.2}$$

Where, $\dot{E}$ is heat transfer rate, h_c is the fluid convection coefficient L is layer thickness, k is thermal conductivity, A is cross-sectional area that heat is flowing across, and ΔT is the temperature gradient. Convection coefficients are not trivial to estimate and can vary significantly. For forced water flow in a pipe, commonly used reference values are in the nominal range of 1000 to 15000 W/m^{2}K for water (Engineers Edge, 2020).

In the case of radial heat flow through a cylinder, steady-state heat transfer through one layer is:

$$\dot{E} = \frac{2\pi kL\Delta T}{\ln(r_o/r_i)} \tag{C.3}$$

Where, r_o is outer radius and r_i is inner radius.

The temperature distribution for the planar (i.e., fracture) and radial (i.e., well) cases will be:

$$T(r) = \begin{cases} \frac{r-r_o}{r_o-r_i}(T_o - T_i) + T_i & \text{if planar} \\ \frac{\ln(r_i/r)}{\ln(r_i/r_o)}(T_o - T_i) + T_i & \text{if radial} \end{cases} \tag{C.4}$$

The thermal conductivity term for convection inside a pipe is stated as:

$$U = 2\pi r_i L h \tag{C.5}$$

Combining, the steady-state heat transfer through a cemented and cased well or a planar rock fracture (Figure 5) is:

$$\frac{d\dot{E_{ro}}}{dL} = \begin{cases} 2\left[\frac{1}{h_c} + \frac{r_d}{k_{rock}}\right]^{-1} w(T_o - T_i) & if\ fracture \\ \left[\frac{1}{2\pi r_a h_c} + \frac{\ln(r_d/r_c)}{2\pi k_{rock}} + \frac{\ln(r_c/r_b)}{2\pi k_{cement}} + \frac{\ln(r_b/r_a)}{2\pi k_{steel}}\right]^{-1}(T_o - T_i) & if\ well \end{cases} \tag{C.6}$$

Next, energy withdraw from the rock can be stated by:

$$\dot{E} = \frac{dE}{dt} \tag{C.7}$$

Or alternatively as:

$$E_{t+1} = \int \dot{E}_t dt + E_t \tag{C.8}$$

Here we must solve the integral for total energy withdraw per unit of length along the axis of flow. The fractures and wells will have negligible temperature gradients along the length, so axial heat transfer will be neglected. It can also be shown that the cement, casing, and fluid convection terms are negligible for heat transfer in the long term (more than 1 yr) because the heat transfer will be severely limited by the thermal conductivity of the rock, so we can ignore those terms. This gives us the following,

$$\frac{dE_{ro}}{dl} = \begin{cases} \frac{dE_{ro,f}}{dl} & if\ fracture \\ \frac{dE_{ro,w}}{dl} & if\ well \end{cases} \tag{C.9}$$

$$\frac{dE_{ro,f}}{dl} = wS_v(T_d - T_a)r_d \tag{C.10}$$

$$\frac{dE_{ro,w}}{dl} = 2\pi S_v(T_d - T_a)\left(\frac{((1-\ln(r_c))/\ln(r_c/r_d))(r_d{}^2 + r_c{}^2)}{2} + \frac{r_d{}^2(\ln(r_d)-0.5) - r_c{}^2(\ln(r_c)-0.5)}{2\ln(r_c/r_d)}\right) \tag{C.11}$$

For our solution, we must solve for both the total energy transfer (E_{ro}) with a given 'thermal radius' (r_d) and for the 'thermal radius' with a given total energy transfer. Since the above relationship for a well would be cumbersome to solve for thermal radius, we instead can fit an approximation function using linear regression (Fig. 10) to quantify the constants (c_1 and c_2) in:

$$\ln(r_d) \cong c_1 \ln\left(\frac{dE_{ro,w}}{dl\Delta T}\right) + c_2 \tag{C.12}$$

$$\frac{dE_{ro,w}}{dl} = (T_d - T_a)e^{(\ln(r_d)-c_2)/c_1} \tag{C.13}$$

From the above relationships, we can now estimate the thermal radius or total energy withdraw for the rock at any time after flow begins through a fractured system. This solution can predict transient heat transfer effects by tracking the total energy withdraw from the rock over time. This does not require a constant internal fluid temperature, so thermal breakthrough can be predicted.

2.6.2 Explicit Heat Transfer Solver:

As the thermal radius approaches zero, the thermal conduction will approach infinity. To mitigate this instability, the model starts by assuming thermal withdraw from a small thickness zone around the wells and fractures. For each pipe, we estimate this by:

$$E_{t0} = \begin{cases} \Delta E_0 wL & \text{if fracture} \\ 2\pi\Delta E_0 r_c L & \text{if well} \end{cases} \tag{D.1}$$

Where, ΔE_0 is a user selected initial energy withdraw that yields a stable model output as determined by trial and error. Our nominal value for ΔE_0 is 500 kJ/m^2 when fracture lengths are 500 m and timesteps are 1 yr.

Next, the initial energy withdraw is used to obtain an initial thermal radius for heat conduction as (Eqns. C.10 & C.13):

$$r_d = \begin{cases} \frac{E_{t0}}{S_v wL\Delta T} & \text{if fracture} \\ e^{c_1 \ln\left(\left|\frac{E_{t0}}{L\Delta T}\right|\right)+c_2} + r_c & \text{if well} \end{cases} \tag{D.2}$$

Which then yields the initial rate of thermal conduction for the timestep (Eq. C.6):

$$\dot{E}_t = \begin{cases} 2\left[\frac{1}{h_c} + \frac{r_d}{k_{rock}}\right]^{-1} wL\Delta T & \text{if fracture} \\ \left[\frac{1}{2\pi r_a h} + \frac{\ln(r_d/r_c)}{2\pi k_{rock}} + \frac{\ln(r_c/r_b)}{2\pi k_{cement}} + \frac{\ln(r_b/r_a)}{2\pi k_{steel}}\right]^{-1} L\Delta T & \text{if well} \end{cases} \tag{D.3}$$

Next in the timestep, nodal temperatures are computed using the result from the flow model, fluid mixing at nodes, and fluid enthalpy data as dependent on temperature, pressure, and steam quality. This yields information on the heat that can be absorbed by the fluid, which can be less than the amount of heat that the rock can conduct to the fluid at a given temperature gradient. Thus, the energy extracted in a timestep becomes:

$$E_{t+1} = \left|\dot{E_p}\right|\Delta t + E_t \tag{D.4}$$

Where, E_p is the energy transferred to or from the fluid in the timestep. The absolute value of this term is used to prevent numerical instability that can occur if heating changed to cooling, or vice versa, during timesteps. This new value allows us to update the thermal radius and heat transfer rates for the next timestep by repeating Eqns. (D.2 & D.3). If no heat was transferred on a given segment (e.g., $\Delta T = 0$), the values from the previous time step are used again.

2.6.3 Iterative Nodal Temperature Solver:

As mentioned earlier, the nodal temperatures are initialized at the in-situ equilibrium rock temperature. Overriding this, the inlet, outlet, and/or boundary temperatures can be specified. The enthalpy and other fluid properties at these nodes can then be calculated from steam tables. At the end of the timestep, these temperatures are updated by considering heat transfer to and from the fluid and mixing of flow streams into nodes. This requires an iterative process because of the initial guess of temperatures. The first part of iteration calculates heat flow and a second part calculates mixing, to update node temperatures. With the new node temperatures, the next iteration is run until temperature changes between iterations reduced to an acceptably small value.

Our explicit solver uses large timesteps (Δt) to rapidly solve for network heat transfer. This can be on the order of 1 yr or perhaps even larger. To support these large steps, we consider the rock's heat deliverability and the fluid's heat capacity across each flow segment. In a timestep, this requires solving the following set of equations:

$$A = \dot{E}_t\left(T_d - 0.5\left(T_{nj} + T_{ni}\right)\right) \tag{E.1}$$

$$B = \dot{E}_t\left(T_d - 0.5(T_d + T_{ni})\right) \tag{E.2}$$

Frash

$$C = \frac{Q_{ij}}{v}\left(h_{eqj} - h_{ni}\right) \tag{E.3}$$

Where, A is rock conduction along a segment where both the upstream and downstream nodes are out of equilibrium with the adjacent rock temperature. B is rock conduction where only the upstream node is out of equilibrium. C is fluid enthalpy change if the downstream node is at equilibrium. h is fluid enthalpy as determined from the pressure, temperature, and steam quality (IAPWS, 1997). Also, v is specific volume at a reference enthalpy that we take from the injection well's fluid inlet state, i is the upstream node of the segment, j is the downstream node of the segment, and eqj is the equilibrated state at the downstream segment. Which of A, B, or C occurs depends on the most limiting term:

$$X = \max(A, B) \tag{E.4}$$

$$\dot{E_p} = \min(X, C) \tag{E.5}$$

Now that we know the limiting heat transfer factor for the segment, we can calculate the enthalpy at the downstream node as:

$$h_j = \dot{E_p} + \frac{Q_{ij}}{v} h_i \tag{E.6}$$

We can then use the mixed inflowing enthalpy for each node to obtain an updated nodal enthalpy by:

$$h_n = \left(\sum \frac{Q_{ij}}{v} h_j / \sum \frac{Q_{ij}}{v}\right)\Big|_{inflow} \tag{E.7}$$

$$T_n = f(h_n, P_n) \tag{E.8}$$

Where, h_n is mixed nodal inflow enthalpy and only inflow streams are included in the calculation. By reference to the nodal pressure, this completes the state variables to get nodal temperature, T_n.

2.7 Power Output

A key output from our model is a prediction of the produced fluid enthalpy and flow rate from a leaky EGS reservoir. This provides the required input for thermal-electric power generation estimation. There are many available technologies to convert the high-enthalpy produced water into electrical energy, with common examples including the Flash Rankine Cycle and the Binary or Organic Rankine Cycles. For a first cut at this prediction, we will focus on the Single Flash Rankine Steam Cycle (Figure 7). This provides a low estimate of electrical output potential relative to the full set of options. However, using this cycle helps to reconcile enthalpy and flow rate into an easily understood term of net-energy production.

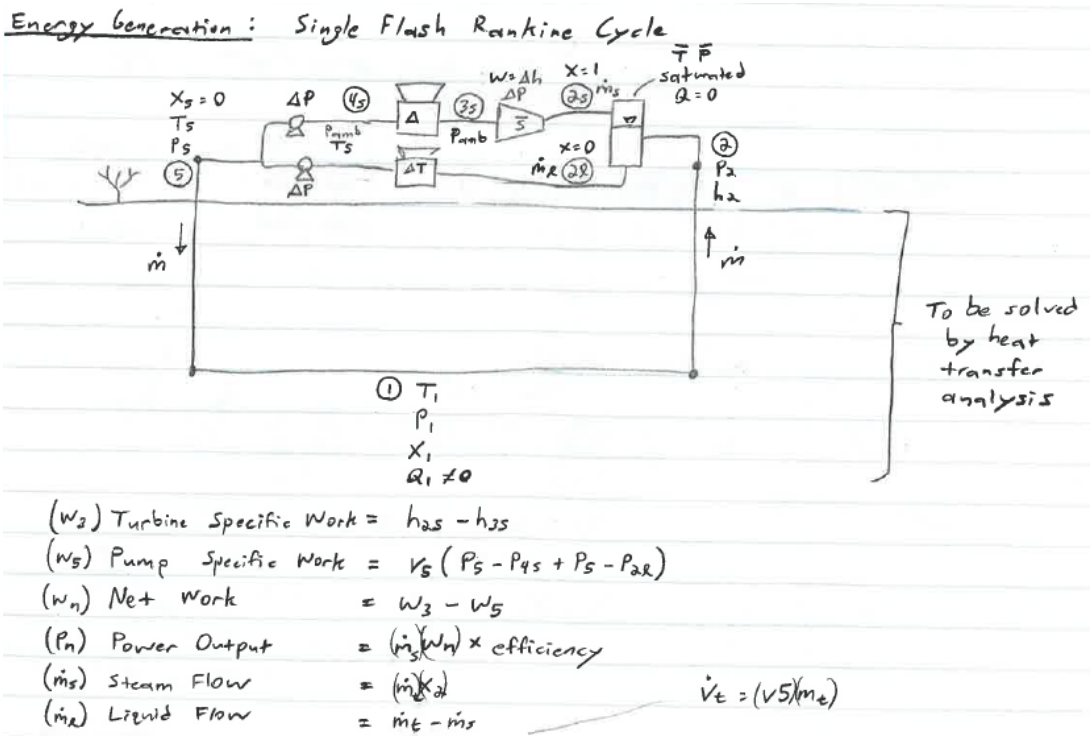

Figure 7: Single flash Rankine cycle used to estimate geothermal to electrical energy production potential.

3. EXAMPLE MODEL RESULTS

This model is ultimately intended as a tool to quickly estimate EGS production as a function of key decisions during development, when a minimum of information is known about the site. Some of these key decisions would likely include:

1. Selecting an optimal placement for all injection and production wells (e.g., well spacing).
2. Selecting optimal production and injection rates for long term reservoir performance.

The primary concerns that will affect these decisions are likely to include:

1. Short-circuiting where one or two fractures dominate flow, resulting in early thermal breakthrough and reduced project life.
2. Poor well connectivity, resulting in high leak-off of the injected fluid and reduced reservoir efficiency.
3. Excessive injection pressures, resulting in reduced net power output, low circulation rates, and induced seismicity.
4. Low produced fluid enthalpy or production flow rate, resulting in reduced energy generation.

We investigate the performance of an injection and production well pair in an EGS reservoir having the base-case properties summarized in Table 1. This table shows the required inputs for our model. The decision making variables we investigate include injection rate and well spacing. The model includes stochastic natural fractures that are sub-vertical striking East. The wells are oriented to the North. The injection well is stimulated with a single hydraulic fracture that is vertical and striking east.

Table 1: Example model input parameters with optional model inputs indicated by shaded boxes.

Parameter	Unit	Mean value	Uncertainty (±)
Domain size (i.e., cubic side length)	m	1600	-
Nominal reservoir depth	m	6000	-
Geothermal gradient	K/km	50	-
Rock density	kg/m^3	2700	-
Rock thermal conductivity	W/mK	2.5	-
Rock volumetric specific heat capacity	kJ/m^{3}K	2063	-
Ambient surface temperature	C	25.0	-
Ambient surface pressure	MPa	0.101	-
Cement thermal conductivity	W/mK	2.0	-
Cement volumetric specific heat capacity	kJ/m^{3}K	2000	-
Electrical generator efficiency	%	85	-
Project lifespan	yr	20	-
Thermal analysis timestep	yr	1.0	-
Casing inner radius	m	0.0762	-
Casing outer radius	m	0.0889	-
Borehole radius	m	0.1016	-
Borehole thermal convection coefficient	W/m^{2}K	3000	-
Hazen-Williams friction coefficient	-	80.0	-
Water density for flow analysis	kg/m^3	980.0	-
Water dynamic viscosity	cP	0.9	-
Reservoir pore pressure	MPa	57.7	-
Reservoir temperature	C	325.0	-
Well spacing	m	360	-
Well length	m	600	-
Well azimuth	deg	324.0	-
Well dip	deg	0.0	-
Natural fracture count	fractures	20	-
Natural fracture diameter	m	550.0	350.0
Natural fracture strike	deg	79.0	16.0
Natural fracture dip	deg	90.0	15.0
Hydraulic fracture count	fractures	1	-
Hydraulic fracture diameter	m	1266.0	214.0
Hydraulic fracture strike	deg	65.0	8.0
Hydraulic fracture dip	deg	57.5	7.5
Fracture aperture (all)	m	0.0002	0.0001
Injection rate	m^3/s	0.002	-
Injection temperature	C	95	-
Production wellhead pressure	MPa	1.0	-

The fracture and borehole system generated for our example is shown in Figure 8. In this scenario, the model predicts that the injection and production rates will be nearly equal, but there is some injected fluid leak-off to the boundary via the natural fractures. Most of the flow travels through the hydraulic fracture from the injection well to the production well.

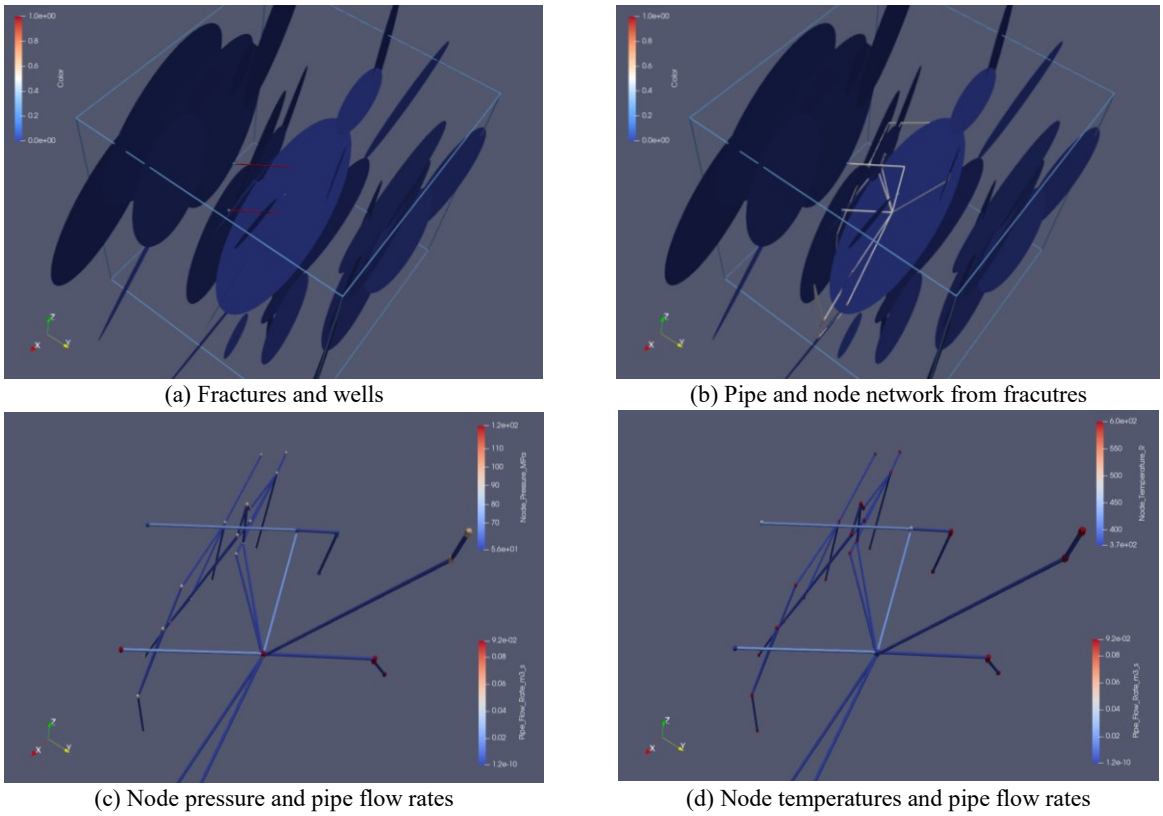

(a) Fractures and wells

(b) Pipe and node network from fracutres

(c) Node pressure and pipe flow rates

(d) Node temperatures and pipe flow rates

Figure 8: Example model prediction of flow, pressure, and fluid temperatures for a pair of wells in a fractured network.

More crucially, the model predicts thermal breakthrough and net electrical power output (Figure 9). As expected, the solution predicts earlier thermal breakthrough with increasing injection rates. In this example, thermal breakthrough within the first 20 yrs requires a flow of only 0.005 m^3/s (5 kg/s). However, the optimal flow rate for power generation is higher at around 0.020 m^3/s (20 kg/s), despite thermal breakthrough occurring sooner.

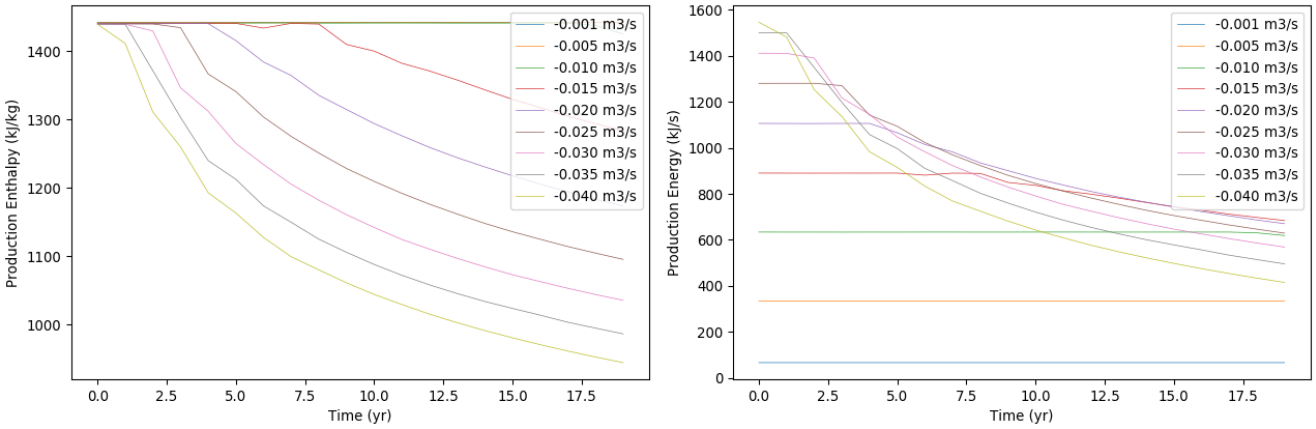

Figure 9: Predicted produced fluid properties as a function of injection rate in a fracture network. The production energy (electrical output) clearly shows an optimal injection flow rate for maximized power output.

To address borehole placement, we apply our model to investigate well spacing (Figure 10). Here, the model predicts an optimal well spacing of 400 m for a single stochastic realization of natural fractures. This observation agrees with other predictions from high-fidelity models for the Utah-FORGE site (Asai, 2018). However, unlike the prior work, our model adds in the complication of fluid loss to the environment and changes the context for design evaluation from rate-enthalpy output to electrical power generation. Predicting the power output enables a more intuitive identification of the decision-making factors that will lead to an improved EGS design.

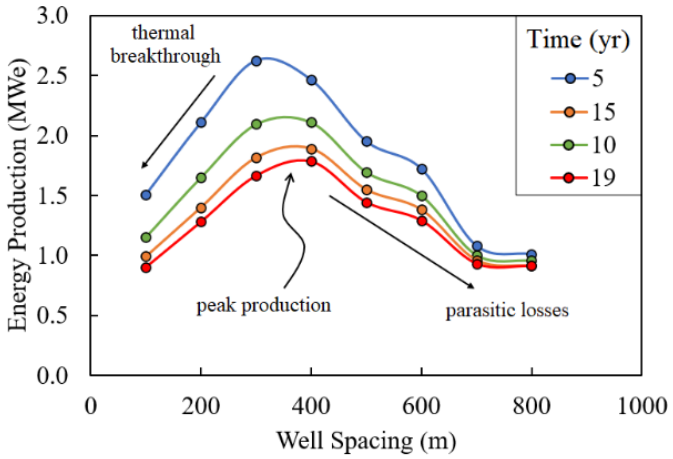

Figure 10: Net electrical energy production from a Single Flash Rankine Cycle with different spacing between parallel wells. This result predicts that close spacing will cause thermal breakthrough to arrive too early. On the other hand, large well spacing will increase fluid loss and pumping costs. Results show an optimal injection rate in the range of 0.001 to 0.065 m^3/s.

4. CONCLUSIONS

Here we present the workings of a fast numerical model that is intended as a tool to aid decision making in the early stages of EGS site development. This tool is not meant to compete with or replace the available high-fidelity numerical models that will undoubtedly be more accurate. Instead, our model is meant to help its users quickly identify reasonable parameters for key design decisions when the uncertainties are high and site information is poor. Often, this situation arises early in a project when no deep wells have yet been drilled. When these wells don't yet exist, the characterization of the site will be uncertain so it will not yet be possible to gain the full benefit from more accurate models. Our model uses a single-processor framework to complete model parameterization, mesh generation, solve flow, solve heat transfer, and estimate net electrical power output. All these steps are completed using a desktop computer in our target of less than 5 minutes for the model above with a 1.6 km domain, 21 fractures, 2 wells, a leaky boundary, and 20 years of production.

ACKNOWLEDGEMENTS

This work is supported by Department of Energy (DOE) Basic Energy Sciences under FWP LANLE3W1. The EGS Collab work in this study is supported by the U.S. Department of Energy, Office of Energy Efficiency and Renewable Energy (EERE), Geothermal Technologies Office (GTO) under Contract No. 89233218CNA000001. Research supporting this work took place in whole or in part at the Sanford Underground Research Facility in Lead, South Dakota. The assistance of the Sanford Underground Research Facility and its personnel in providing physical access and general logistical and technical support is gratefully acknowledged.

The Python code for this work was developed using components from the "Fat Crayon Toolkit" (Singh et al., 2019). We gratefully acknowledge all the contributors to the Fat Crayon Toolkit, especially its lead developer Joseph P. Morris.

We also gratefully acknowledge useful feedback from J. William Carey during discussions concerning the development of GeoDT.

EGS Collab Team: J. Ajo-Franklin, T. Baumgartner, K. Beckers, D. Blankenship, A. Bonneville, L. Boyd, S. Brown, J.A. Burghardt, C. Chai, A. Chakravarty, T. Chen, Y. Chen, B. Chi, K. Condon, P.J. Cook, D. Crandall, P.F. Dobson, T. Doe, C.A. Doughty, D. Elsworth, J. Feldman, Z. Feng, A. Foris, L.P. Frash, Z. Frone, P. Fu, K. Gao, A. Ghassemi, Y. Guglielmi, B. Haimson, A. Hawkins, J. Heise, C. Hopp, M. Horn, R.N. Horne, J. Horner, M. Hu, H. Huang, L. Huang, K.J. Im, M. Ingraham, E. Jafarov, R.S. Jayne, T.C. Johnson, S.E. Johnson, B. Johnston, S. Karra, K. Kim, D.K. King, T. Kneafsey, H. Knox, J. Knox, D. Kumar, K. Kutun, M. Lee, D. Li, J. Li, K. Li, Z. Li, M. Maceira, P. Mackey, N. Makedonska, C.J. Marone, E. Mattson, M.W. McClure, J. McLennan, T. McLing, C. Medler, R.J. Mellors, E. Metcalfe, J. Miskimins, J. Moore, C.E. Morency, J.P. Morris, T. Myers, S. Nakagawa, G. Neupane, G. Newman, A. Nieto, T. Paronish, R. Pawar, P. Petrov, B. Pietzyk, R. Podgorney, Y. Polsky, J. Pope, S. Porse, J.C. Primo, C. Reimers, B.Q. Roberts, M. Robertson, V. Rodriguez-Tribaldos, W. Roggenthen, J. Rutqvist, D. Rynders, M. Schoenball, P. Schwering, V. Sesetty, C.S. Sherman, A. Singh, M.M. Smith, H. Sone, E.L. Sonnenthal, F.A. Soom, D.P. Sprinkle, S. Sprinkle, C.E. Strickland, J. Su, D. Templeton, J.N. Thomle, C. Ulrich, N. Uzunlar, A. Vachaparampil, C.A. Valladao, W. Vandermeer, G. Vandine, D. Vardiman, V.R. Vermeul, J.L. Wagoner, H.F. Wang, J. Weers, N. Welch, J. White, M.D. White, P. Winterfeld, T. Wood, S. Workman, H. Wu, Y.S. Wu, E.C. Yildirim, Y. Zhang, Y.Q. Zhang, Q. Zhou, M.D. Zoback

REFERENCES

Asai, P., Panja, P., McLennan, J., and Moore, J.: Performance evaluation of enhanced geothermal system (EGS): surrogate models, sensitivity study and ranking key parameters. *Renewable Energy*, **122**, 184-195 (2018).

Cooper, J.R. and Dooley, R.B.: Revised release on the IAPWS industrial formulation 1997 for the thermodynamic properties of water and steam. *The International Association for the Properties of Water and Steam* (2007).

Engineers Edge: Convective heat transfer coefficients table chart, Accessed on Dec 15, 2020, https://www.engineersedge.com, (2020).

Fischer, T., Hainzl, S., and Dahm, T.: The creation of an asymmetric hydraulic fracture as a result of driving stress gradients, *Geophysical Journal International*, **179**, 634-639, (2009).

Frash, L.P., Welch, N., Carey, J.W.: Progress towards a scaling relationship between shear fracture length, aperture, and permeability. *Proceedings*, 54th US Rock Mechanics/Geomechanics Symposium, Golden, CO (2020).

Jeppson, R.W.: Steady flow analysis of pipe networks: an instructional manual. *Reports*, **300**, (1974).

Kneafsey, T., Blankenship, D., Dobson, P.F., Morris, J.P., White, M. et al.: The EGS Collab Project: learnings from Experiment 1, *Proceedings*, 45th Workshop on Geothermal Reservoir Engineering, Stanford University, Stanford, CA (2020).

Lienhard, J.H.IV, and Lienhard, J.H.V: *A Heat Transfer Textbook, Fifth Edition*. Phlogiston Press, (2019).

Romera, J.J.G.: iapws, Accessed on Apr 2 , 2018, https://github.com/jjgomera/iapws, (2017).

Singh, A., Neupane, G., Dobson, P., Zoback, M., Morris, J., Fu, P., et al.: Slip tendency analysis of fracture networks to determine suitability of candidate testbeds for EGS Collab hydroshear experiment, *Idaho National Laboratory*, (2019).

Valko, P. and Economides, M.J.: *Hydraulic Fracture Mechanics*, Wiley, (1996).